frontiers in Environmental Chemistry

ORIGINAL RESEARCH
published: 11 May 2021
doi: 10.3389/fenvc.2021.672250

Evaluation of Manganese Oxide Octahedral Molecular Sieves for CO and C_3H_6 Oxidation at Diesel Exhaust Conditions

Xin Wang, Wei Tan, Kai Guo, Jiawei Ji, Fei Gao, Qing Tong* and Lin Dong*

Key Laboratory of Mesoscopic Chemistry of MOE, School of Chemistry and Chemical Engineering, Jiangsu Key Laboratory of Vehicle Emissions Control, School of Environment, Center of Modern Analysis, Nanjing University, Nanjing, China

Mn-based materials have been widely applied in the environmental catalysis field for their excellent redox properties. Here, three kinds of crystallite manganese oxides (pyrolusite, cryptomelane and todorokite) with different tunnel sizes (MnO(1 × 1), MnO(2 × 2), and MnO(3 × 3)) were prepared by hydrothermal method, and their catalytic performance in complete oxidation of diesel vehicle exhaust were tested. The highest catalytic oxidation activity was achieved on MnO(3 × 3) when compared with that on MnO(1 × 1) and MnO(2 × 2). Via a series of characterizations, such as transmission electron microscope, scanning electron microscope, X-ray powder diffraction, N_2-sorption experiments, temperature-programmed reduction by H_2/CO, and X-ray photoelectron spectroscopy, *etc.*, it was found that the catalytic activity was mainly determined by the tunnel structure, specific surface area, and redox ability.

Keywords: manganese oxides, molecular sieves, C_3H_6 oxidation, CO oxidation, diesel oxidation catalyst

OPEN ACCESS

Edited by:
Dengsong Zhang,
Shanghai University, China

Reviewed by:
Yanglong Guo,
East China University of Science and Technology, China
Jian-Wen Shi,
Xi'an Jiaotong University, China
Zhen Zhao,
China University of Petroleum, China

****Correspondence:***
Fei Gao
gaofei@nju.edu.cn
Qing Tong
tongqing@nju.edu.cn

Specialty section:
This article was submitted to Catalytic Remediation, a section of the journal Frontiers in Environmental Chemistry

Received: *25 February 2021*
Accepted: *21 April 2021*
Published: *11 May 2021*

Citation:
Wang X, Tan W, Guo K, Ji J, Gao F, Tong Q and Dong L (2021) Evaluation of Manganese Oxide Octahedral Molecular Sieves for CO and C_3H_6 Oxidation at Diesel Exhaust Conditions. Front. Environ. Chem. 2:672250. doi: 10.3389/fenvc.2021.672250

INTRODUCTION

Diesel vehicles have been widely used due to its less carbon dioxide emissions, higher fuel efficiency, better reliability and durability. However, diesel vehicle engines emit many harmful pollutants, including NO_x, CO, and unburned hydrocarbons (C_xH_y), which are dangerous for both human health and environment. Due to the lean-burn and oxygen-rich conditions, traditional three-way catalyst (TWC) cannot meet the requirements of diesel engine exhaust systems for increasingly stringent government laws and regulations. In decades, many efforts have been devoted to developing diesel exhaust after-treatment systems.

Diesel oxidation catalyst (DOC) is the core of current technologies for controlling diesel vehicle exhaust, which is used to oxidize CO and C_xH_y into non-toxic CO_2 and H_2O, and oxidize NO into NO_2 to accelerate sequential fast SCR reaction (Tan et al., 2021). At present, the most common active components of DOC catalysts in industrial applications are platinum-group metals, such as Pt, Pd, *etc.*, with transition metal oxides such as Al_2O_3 and CeO_2 as supports (Liu et al., 2013; Liu et al., 2015; Raj et al., 2015; Carrillo et al., 2017; Ren et al., 2018; Leistner et al., 2019). Pt-group metals exhibit the excellent removal efficiency on CO, C_xH_y, NO, and other polluting components in diesel vehicle exhaust at low temperatures (Khosravi et al., 2014). There are still some problems with the usage of them, such as the rather expensive, limited reserves, and the susceptibility to sinter causing activity loss at high temperatures. It is significantly demanded to design an efficient noble metal-free DOC catalyst.

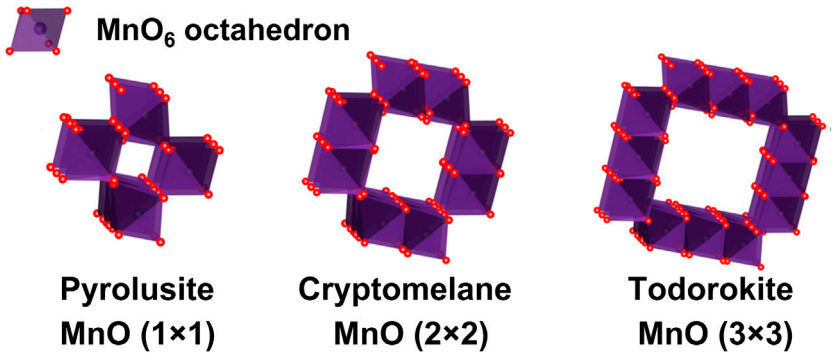

FIGURE 1 | Three typical manganese oxide square tunnel structures.

Among various noble metal-free DOC catalysts, transition metal oxides have received more and more attention, and they are considered to be environmental-friendly catalysts with great potential to replace the precious metals (Wang F. et al., 2012; Heo et al., 2018). Manganese oxide (MnO_x) is one of the most common transition metal oxides. The variable valence of Mn and the superior redox propertie have enabled MnO_x as a promising candidate for efficient DOC catalyst (Kim et al., 2010; Gao et al., 2016; Xu et al., 2006; Shi et al., 2019; Miao et al., 2019; Liu F. et al., 2018). Manganese oxides exist in many crystallines, which can be roughly divided into one-dimensional tunnel structure, two-dimensional layered structure and three-dimensional spinel structure (Huang Z. et al., 2012; Liu P. et al., 2018), manganese oxide with tunnel structure, also named as manganese oxide octahedral molecular sieve, has received extensive attention due to its superior catalytic performance (Makwana et al., 2002; Jarrige and Vervisch, 2009; Huang et al., 2017; Tang et al., 2010; Zhou et al., 2017; Liu Y. et al., 2018; Uematsu et al., 2016; Wang et al., 2017; Tang et al., 2006; Chen et al., 2009). Three typical manganese oxide square tunnel structures (pyrolusite, cryptomelane and todorokite) are shown in **Figure 1**, denoted as MnO(1 × 1), MnO(2 × 2), and MnO(3 × 3), respectively. The [MnO_6] octahedron forms single, double or triple chains through edge and/or angle sharing, then the chains form a square hollow tunnel in an approximately orthogonal manner (Shiley and Buseck, 1981; Shen et al., 2005). For pyrolusite, single chains of edge-sharing [MnO_6] octahedra share corners with neighboring chains to form a framework structure containing tunnels with square cross sections that are one octahedron by one octahedron (1 × 1) on one side, forming a framework structure containing approximately 0.23 × 0.23 nm^2 tunnels (MnO(1 × 1)) (Ooi et al., 1987). The microstructure of cryptomelane is constructed of double chains of edge-sharing [MnO_6] octahedra, but they are linked in such a way as to form tunnels with square cross sections about 0.46 × 0.46 nm^2, measuring two octahedra on a side (MnO(2 × 2)) (Brock et al., 1998; Qi et al., 1999). The tunnel in todorokite is composed of [MnO_6] octahedrons with three edges sharing chains, forming a frame structure of about 0.69 × 0.69 nm^2 tunnel (MnO(3 × 3)) (Golden et al., 1985; Shen et al., 1993; Ching and Roark, 1997). Their structural frameworks are similar to zeolite (Shiley and Buseck, 1981; Ooi et al., 1987; Qi et al., 1995). Many studies have confirmed the tunnel structure of manganese oxide is similar to molecular sieve through different methods. (Fleischer and Richmond, 1943; Breck, 1974; Kijima et al., 2004; Liu P. et al., 2018). However, although the unique microstructure of MnO_x tunnels have arose great interests of researchers, few studies on revealing the impact of tunnel structure effect over MnO_x as DOCs on their catalytic performance have been reported.

Herein, three different tunnel structure catalysts were prepared by a hydrothermal method, and the influence of the tunnel structure over on the catalytic activity of diesel vehicle exhaust gas (CO, C_3H_6) oxidation was studied. Via a series of characterizations, such as X-ray powder diffraction (XRD), transmission electron microscope (TEM), scanning electron microscope (SEM), nitrogen adsorption and desorption experiments (N_2-sorption), temperature programmed reduction by CO (CO-TPR), temperature programmed reduction by H_2 (H_2-TPR), and X-ray photoelectron spectroscopy (XPS), a structure-performance relationship has been established where the tunnel structure, as well as the redox properties of manganese oxide, determined the catalytic oxidation activity. The present result is expected to give a promising pathway for the design and preparation of the low-cost efficient DOCs that are entirely noble metal-free.

EXPERIMENTS

Materials

Analytical grade hydrate $MnSO_4{\cdot}H_2O$, $MnCl_2.4H_2O$ $(NH_4)_2S_2O_8$, and NaOH were purchased from Sinopharm Chemical Reagent, Co., Ltd., China. $KMnO_4$ was purchased from Nanjing Chemical Reagent, Co., Ltd., China. $MgCl_2{\cdot}6H_2O$ was obtained from Shanghai Macklin Biochemical Co., Ltd., China. Deionized water was used throughout the experiment process.

Catalysts Preparation

The MnO(1 × 1) and MnO(2 × 2) manganese oxides were prepared by a redox hydrothermal method according to the following reaction **Eqs. 1**, **2**, respectively (Wang and Li, 2002):

$$S_2O_8^{2-} + Mn^{2+} + 2H_2O \rightarrow 2SO_4^{2-} + MnO_2 + 4H^+ \; E^{\Theta} = 0.786\,V \quad (1)$$

$$2MnO_4^- + 3Mn^{2+} + 2H_2O \rightarrow 5MnO_2 + 4H^+ \; E^{\Theta} = 0.455\,V \quad (2)$$

A certain amount of manganese sulfate ($MnSO_4{\cdot}H_2O$ (2.91 g)) and an equal amount of ammonium persulfate ($(NH_4)_2S_2O_8$ (3.93 g)) were dissolved in distilled water (40 mL) at room temperature under vigorous magnetic stirring, then the homogeneous solution was transferred into a Teflon-lined stainless steel autoclave, sealed, and maintained at 160°C for 24 h. The obtained black solid product was filtered, washed with distilled water to remove ions possibly remaining in the final products, and finally dried at 110°C overnight. The whole process, appropriate for the preparation of pyrolusite, was conveniently adjusted to prepare MnO(2 × 2) by simply adding analytical grade $KMnO_4$ (1.66 g) instead of $(NH_4)_2S_2O_8$ to the reaction system.

The MnO(3 × 3) manganese oxide was prepared through the precipitation method according to the reported literature (Breck, 1974). Briefly, birnessite was initially synthesized by the coprecipitation method. Manganese dichloride ($MnCl_2{\cdot}4H_2O$ (3.96 g)) and $MgCl_2{\cdot}6H_2O$ (1.63 g) were dissolved in 40 mL deionized water to form a mixed solution, in which the 5.0 M NaOH (50 mL) and 0.20 M $KMnO_4$ (40 mL) solutions were successively added. The mixture was stirred for 30 min and aged at room temperature for 48 h and then washed with the deionized water to obtain Na-birnessite. MnO(3 × 3) was prepared by the addition of the Na-birnessite above into 1 L of 1.0 M $MgCl_2$, and stirred for 12 h at room temperature. The sample was then centrifuged and washed three times with a large amount of distilled deionized water, then charged into Teflon-lined autoclaves at 150°C for 48 h. The resulting solid product was filtered, washed with the deionized water and dried at 110 °C overnight. The manganese oxides were obtained by calcining the dried samples above in air at 300°C for 6 h and denoted as MnO(1 × 1), MnO(2 × 2), and MnO(3 × 3), respectively, according to the properties of their tunnels for clarity.

Catalysts Characterizations

Transmission electron microscopy (TEM) images were taken on a JEM-1011 instrument at an acceleration voltage of 200 kV. The sample was dispersed in A.R. grade ethanol with ultrasonic treatment and the resulting suspension was allowed to dry on a carbon film supported on copper grids. The morphologies of samples were observed via a field-emission scanning electron microscope (JSM-6701F, JEOL accelerating voltage of 5 kV).

X-ray diffraction patterns were recorded on a Philips X'pert Pro diffractometer using Ni-filtered Cu Kα radiation source (λ = 0.15 nm) at 40 kV and 30 mA under ambient conditions. The scan angle extended from 10° to 90° using a step size of 0.02°, and scan speed was 10 min^{-1}.

N_2 adsorption-desorption isotherms were carried out on a Micromeritics ASAP 2020 instrument using nitrogen gas as an adsorbate at 77 K. Before measurement, the samples were vacuum-pretreated at 200°C for 3 h. The Brunauer-Emmett-Teller (BET) equation and the Barrett-Joyner-Halenda (BJH) method were applied for the measurement of the specific surface area and the pore size distribution, respectively.

X-ray photoelectron spectroscopy (XPS) measurements were conducted using a PHI 5000 Versa Probe system with a monochromatic Al Kα radiation (1486.6 eV, 15 kW). All binding energies were calibrated by the adventitious C 1s (284.6 eV) to compensate for surface charge effects. This reference gave BE values with accuracy at ± 0.1 eV. All the data were analyzed by XPS PEAK software using Shirley type background.

Inductively coupled plasma atomic emission spectroscopy (ICP-AES) was used for elemental analysis on a Perkin Elmer Optima 5300DV instrument with a radiofrequency power of 1300 W. The sample was dispersed in a mixture of HNO_3 and H_2SO_4 (volume ratio 1:3) before the determination of their chemical compositions and treated by ultrasonic for 1 h to get the sample completely dissolved in the liquid phase.

Temperature programmed reduction by H_2 (H_2-TPR) experiments were carried out in a quartz U-tube reactor connected to a TCD with a H_2/Ar mixture (7% H_2 by volume) as a reductant. 10 mg sample was used for each measurement. Before introducing the sample to the H_2/Ar stream, the sample was pretreated in a N_2 stream (50 mL/min) at 150°C for 1 h. The H_2 consumption profiles were collected from room temperature to 800°C at a rate of 10°C/min.

CO temperature-programmed reduction (CO-TPR) experiments were conducted in a quartz tube with 30 mg catalyst loaded. The sample was pretreated in Ar stream (200 mL/min) at 120°C for 0.5 h before reduction and then cooled to room temperature. After that, CO/He mixture was switched on and the sample was heated from room temperature to 650°C with a heating rate of 10°C min^{-1}. The effluent gases including CO and CO_2 were continuously analyzed by an online LC-D series mass spectrometer.

Catalytic Activity Tests

Catalytic activity tests for C_3H_6 or CO oxidation were carried out on a fixed-bed continuous flow quartz reactor. The feeding gas contains 1% C_3H_6 (or CO)/He, 20% O_2/He with a total flow rate of 10 mL min^{-1}. In each test, 50 mg sample was used and the weight hourly space velocity (WHSV) was 12,000 mL $g^{-1}{\cdot}h^{-1}$. Before switching on the reactant flow, the sample was pretreated in a flowing He stream at a rate of 20 mL/min at 150°C for 0.5 h to remove the adsorbed impurities. After that, the sample was cooled to room temperature and exposed to reactant gases until reaching saturated adsorption. The oxidation activity was tested under steady conditions. The outlet gas composition was measured by an online GC-9860 gas chromatograph equipped with TCD and FID detectors. C_3H_6 and CO conversion were calculated by the following equations:

$$C_3H_6 \text{ coversion } (\%) = \left(1 - \frac{[C_3H_6]_{out}}{[C_3H_6]_{in}}\right) \times 100\%$$

$$CO \text{ coversion } (\%) = \left(1 - \frac{[CO]_{out}}{[CO]_{in}}\right) \times 100\%$$

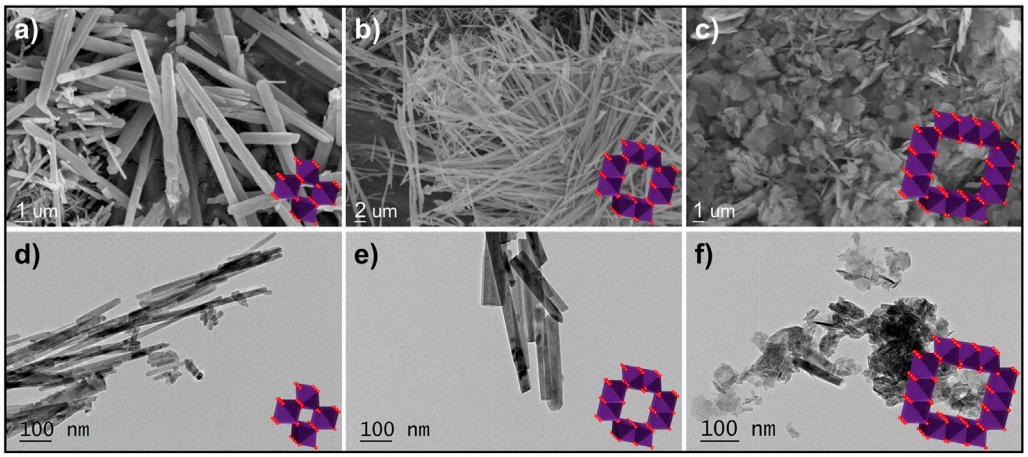

FIGURE 2 | TEM and SEM images of MnO(1 × 1) **(A,D)**, MnO(2 × 2) **(B,E)**, and MnO(3 × 3) **(C,F)**.

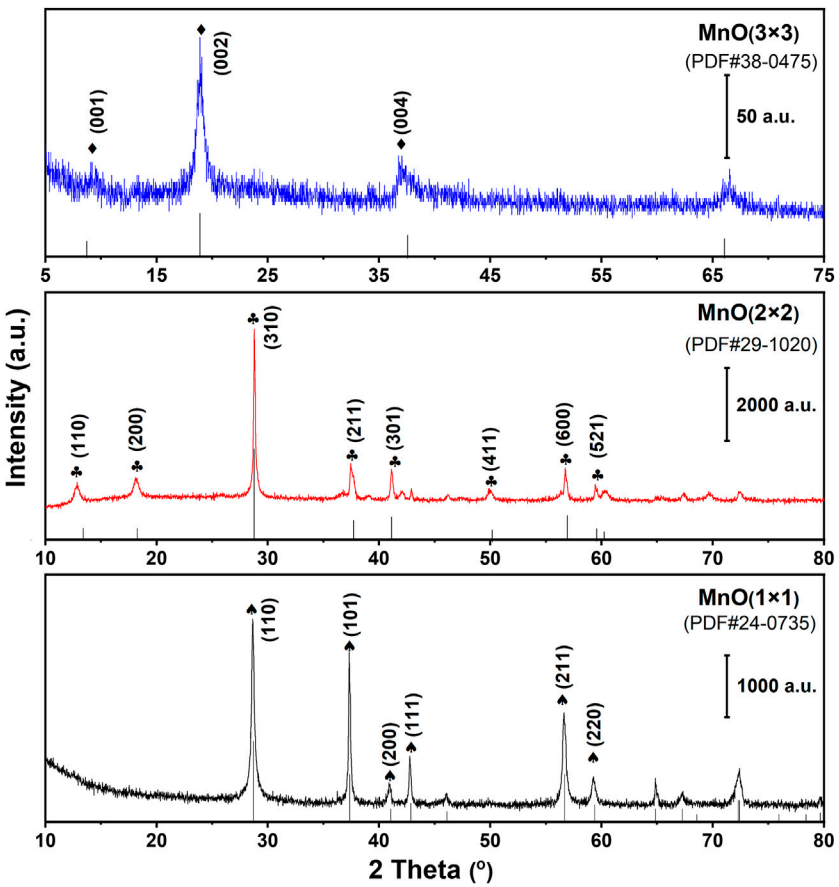

FIGURE 3 | XRD patterns of MnO(1 × 1), MnO(2 × 2), MnO(3 × 3).

where $[C_3H_6]_{in}$ and $[CO]_{in}$ represent the initial C_3H_6 and CO concentrations, $[C_3H_6]_{out}$ and $[CO]_{out}$ represent the residual C_3H_6 and CO concentrations, respectively.

The light-off experiments of CO and C_3H_6 simultaneous oxidation activity performance of various catalysts were evaluated in a fixed-bed quartz reactor (8 mm internal

TABLE 1 | The textural properties of various catalysts.

Sample	SSA (m^2/g)	Pore volume (cm^3/g)
MnO(1 × 1)	15.3	0.05
MnO(2 × 2)	33.6	0.11
MnO(3 × 3)	68.3	0.33

diameter) operating with a steady state flow. The feed stream was fixed with 200 ppm CO, 200 ppm C_3H_6, 10% O_2, and the total gas flow is controlled at 100 mL/min. In each test, 100 mg sample was used and the weight hourly space velocity (WHSV) was 60,000 mL $g^{-1}{\cdot}h^{-1}$. Before the test, it was pretreated in purified N_2 stream at 150°C for 0.5 h to avoid surface impurities. Then the mixed gases were switched on and the activity data were collected at every target temperature after stabilizing for 30 min. The concentration of effluent gases was continuously analyzed on an MKS MultiGas 6030 FTIR spectrometer equipped with a 2 m path-length gas cell (2 L volume). The C_3H_6 and CO conversion were calculated by the equations shown above.

RESULTS AND DISCUSSION

Structure Characterizations

As shown in **Figure 2**, MnO_x samples synthesized by different methods exhibited significantly different morphologies. MnO(1 × 1) and MnO(2 × 2) displayed uniform shapes of nanowire and nanorod. While the MnO(3 × 3) showed a uniform petal-like shape. The morphologies of the samples were consistent with previous reports (Wang and Li, 2002; Kijima et al., 2004).

To determine the crystalline structure of MnO(1 × 1), MnO(2 × 2), and MnO(3 × 3), the XRD patterns were collected (**Figure 3**). The XRD patterns of the MnO(1 × 1) could be readily indexed to the pure pyrolusite with a tetragonal structure (β-MnO_2, JCPDS 24-0735). While the diffraction peaks of MnO(2 × 2) were attributed to the crystalline phase of cryptomelane (α-MnO_2, JCPDS 29-1020) with a tetragonal structure. For MnO(3 × 3) the diffraction peaks were ascribed to the orthorhombic phase of the todorokite MnO_2 (JCPDS 38-0475).

The specific surface area (SSA) of MnO(1 × 1), MnO(2 × 2) and MnO(3 × 3) were characterized by N_2 adsorption-desorption isotherms and the result were listed in **Table 1**. MnO(3 × 3) (68.3 m^2/g) exhibited a higher SSA than MnO(1 × 1) (15.3 m^2/g), and MnO(2 × 2) (33.6 m^2/g). Compared to MnO(1 × 1) (0.05 cm^3/g) and MnO(2 × 2) (0.11 cm^3/g) samples, higher total pore volume was also achieved on MnO(3 × 3) (0.33 cm^3/g). When combined with the results of SEM, the stacking-type pores of petal-like morphology might account for the higher SSA and larger pore volume of MnO(3 × 3). Liu et al. found that the tunnels in MnO(1 × 1) were too small to accommodate other chemical species, and chemical analysis indicates that the composition of MnO(1 × 1) only slightly deviated from pure MnO_2 (Liu P. et al., 2018). Wang et al. (Wang and Li, 2002) examined the structure and pore properties of MnO(2 × 2) by adsorbing different gases with different molecular diameters. Both H_2O and NH_3 with diameters below 0.265 nm could be inserted into the tunnel structure of MnO(2 × 2), whereas N_2, O_2, Ar, CO, and CO_2 with diameters above 0.33 nm were excluded from the structure. As reported by Shen et al. (Shen et al., 1993), MnO(3 × 3) with a tunnel size of 0.69 nm showed satisfactory adsorptive capacity for C_6H_{12} and CCl_4 with size dimensions of 0.61 and 0.69 nm, respectively. Such a special structure made MnO(3 × 3) exhibit a superior oxidation activity for hydrocarbons.

Catalytic Activity of CO and/or C_3H_6 Oxidation

C_3H_6 oxidation and CO oxidation reactions were selected to evaluated the catalytic oxidation activity of MnO(1 × 1), MnO(2 × 2), and MnO(3 × 3). As shown in **Figure 4**, for the non-catalyst test, the T20 of CO is about 300°C and the T20 of C_3H_6 is about 350°C, which should be due to the ordinary thermal oxidation. The catalytic performances have been significantly improved after loading the catalyst. MnO(3 × 3) shows extremely high catalytic activity for the oxidation of C_3H_6, which achieved a C_3H_6 conversion of 50% at ca. 110°C and a completely oxidation at *ca.* 170°C. However, the C_3H_6 conversions over MnO(1 × 1) and MnO(2 × 2) are only *ca.* 5% at 110°C. Under the same conditions, the temperatures required for the complete oxidation of C_3H_6 over MnO(1 × 1) and MnO(2 × 2) are 320 and 240°C, respectively. Interestingly, their CO oxidation activities are almost the same.

Light-off experiments of CO and C_3H_6 simultaneous oxidation at higher WHSV were also carried out to further estimate the catalytic oxidation activity of MnO(1 × 1), MnO(2 × 2), and MnO(3 × 3) to approach the practical instance. As shown in **Figure 5**, the light-off temperatures of CO and C_3H_6 oxidation on these three MnO_x catalysts shifted to the high temperature, which should be due to the different reaction conditions, especially the increasing of the WSHV from 12,000 to 60,000 mL $g^{-1}{\cdot}h^{-1}$. MnO(3 × 3) catalyst still showed the best C_3H_6 oxidation activity. Interesting, in the presence of C_3H_6, MnO(3 × 3) exhibited much better CO oxidation activity than MnO(2 × 2) and MnO(1 × 1), which was quite different from the results of CO oxidation without C_3H_6 in the reactant. The catalytic performance of some typical catalysts for the oxidation of CO and propylene were listed in **Table 2** (Seo et al., 2021; Li et al., 2019; Ma et al., 2018; Li et al., 2021; Hazlett et al., 2017; Wang et al., 2019; Rida et al., 2006; Tan et al., 2020; Liu et al., 2020; Březina et al., 2020). It was seen that noble metal catalysts had outstanding low-temperature activity below 250°C, while the catalytic activity of transition metal catalysts was generally lower than that of noble metal catalysts. Even though MnO(3 × 3) still shown the comparable catalytic performance. In short, MnO(3 × 3) was a superior catalyst for CO and C_3H_6 oxidation, which made it a promising candidate as a diesel oxidation catalyst. To reveal the reasons for the higher oxidation activity of MnO(3 × 3), a series of physiochemical characterizations were carried out.

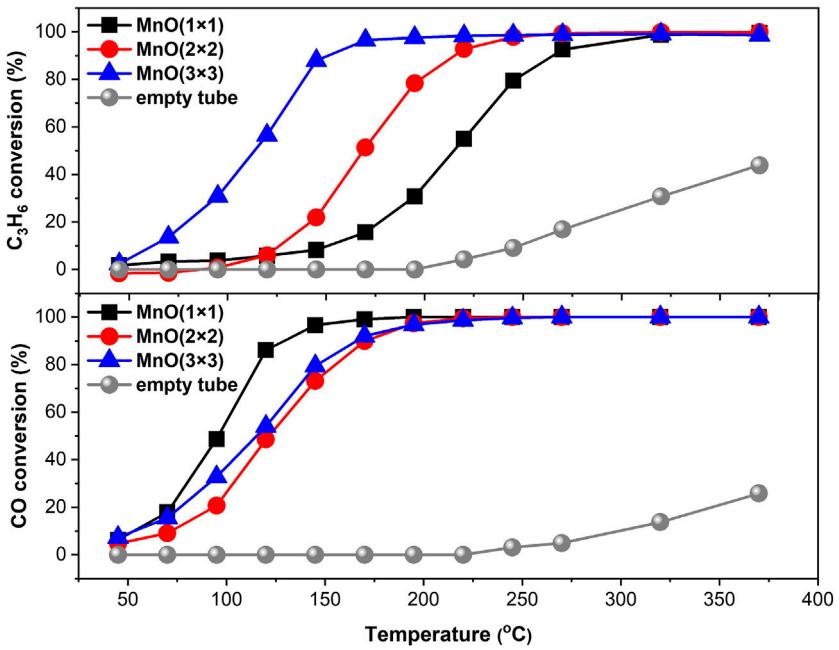

FIGURE 4 | C_3H_6 oxidation and CO oxidation tests of three manganese oxides or non-catalyst. Reaction conditions: 5000 ppm C_3H_6(CO), 10% O_2, He balanced, WSHV of 12,000 ml $g^{-1}{\cdot}h^{-1}$.

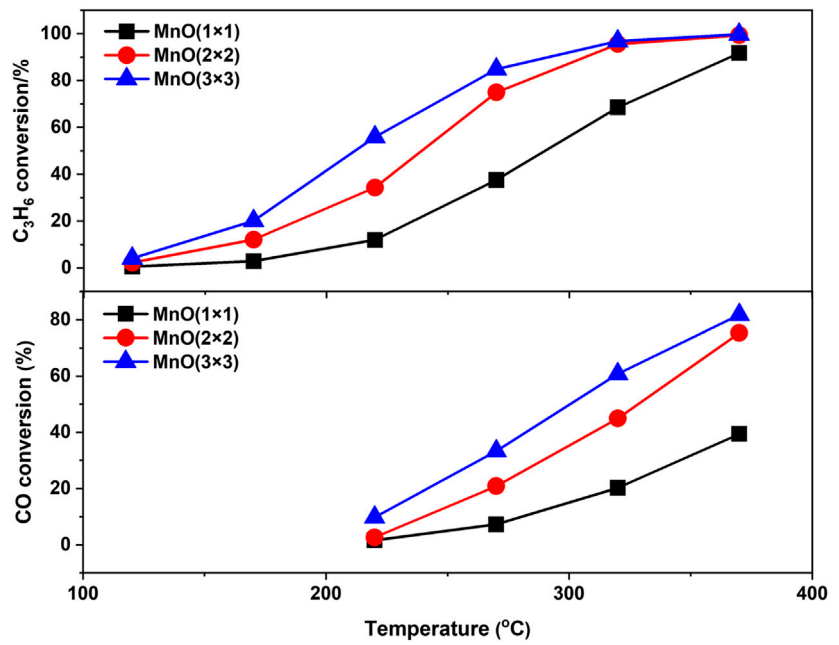

FIGURE 5 | C_3H_6 oxidation and CO oxidation tests of three manganese oxides. Reaction conditions: 200 ppm C_3H_6, 200 ppm CO, 500 ppm NO, 10% O_2, N_2 balanced, WSHV of 60,000 ml $g^{-1}{\cdot}h^{-1}$.

The Redox Property (H_2-TPR, CO-TPR)

H_2-TPR was used to investigate the redox ability of these catalysts. The reduction profiles was shown in **Figure 6**, and the quantitative results of the H_2-consumption peaks in the process of reduction were listed in **Table 3**. For all three MnO catalysts, there were two H_2-consumption peaks in each H_2-TPR

TABLE 2 | The catalytic properties of CO and C_3H_6 oxidation reactions over some typical catalysts.

Catalyst	CO conversion (Temperature)	C_3H_6 conversion (Temperature)	Reaction conditions	References
Pd/Ag-CeO (2 wt% Pd, 0.3 mol% Ag)	90% (169°C)	90% (174 C)	1% CO, 1000 ppm C_3H_6, 10% O_2, WHSV = 120,000 ml/g h	Seo et al. (2021)
CeO_2-Co_3O_4	50% (72°C)	50% (192 C)	0.4% CO, 10% O_2, WHSV = 240, 000 ml g^{-1} h^{-1} 0.1% C_3H_6, 10% O_2, WHSV = 240, 000 ml g^{-1} h^{-1}	Li et al. (2019)
La_2O_3-Co_3O_4	50% (109°C)	50% (226°C)	0.4% CO, 10% O_2, WHSV = 240, 000 ml g^{-1} h^{-1} 0.1% C_3H_6, 10% O_2, WHSV = 240, 000 ml g^{-1} h^{-1}	Li et al. (2019)
Co_3O_4-In_2O_3	100% (90°C)	100% (250°C)	1% CO, 1.5% O_2, WHSV = 240, 00 ml g^{-1} h^{-1}	Ma et al. (2018)
$La_{0.9}Sr_{0.1}CoO_3$	50% (146°C)	50% (258°C)	0.4% CO, 10% O_2, WHSV = 240, 000 ml g^{-1} h^{-1} 0.1% C_3H_6, 10 %O_2, WHSV = 240, 000 ml·g^{-1} h^{-1}	Li et al. (2021)
Pt-Pd/Al_2O_3 (1wt% Pt,0.55wt% Pd)	100% (170°C)	100% (210°C)	3000 ppm CO, 8% O_2, 1500 ppm C_3H_6, 8% O_2	Hazlett et al. (2017)
Pt/La-Al_2O_3 (0.5wt% Pt)	80% (275°C)	100% (300°C)	5000 ppm CO, 500 ppm HCs, 1.0% O_2, 5% H_2O, 1,500,000 cm^3·g_{cat}^{-1} h^{-1}	Wang et al. (2019)
$LaSrCrO_3$	100% (400°C)	100% (367°C)	1% CO, 2% O_2, W/F = 9×10^{-2} s g_{cat} mL^{-1} 0.1% C_3H_6, 1.8% O_2, W/F = 9×10^{-2} s g_{cat} mL^{-1}	Rida et al. (2006)
Pt/CeO_2/Al_2O_3	50% (170°C)	100% (250°C)	1.0% CO, 1.0% O_2, WHSV = 200,000 ml/(g_{cat} h) 2000 ppm C_3H_6, 2% O_2, WHSV = 200,000 ml/(g_{cat} h)	Tan et al. (2020)
$LaMnCoO_3$	—	100% (250°C)	1000 ppm C_3H_6, 3%O_2, 5%H_2O, WHSV = 240,000 cm^3 g^{-1} h^{-1}	Liu et al. (2020)
Pt/CeO_2/γ-Al_2O_3 (2.3wt % Pt)	100% (250°C)	100% (300°C)	1660 ppm CO, 6.584% O_2, 860 ppm C_3H_6, 7% H_2O, 7% CO_2, 600 ppm NO, GHSV = 50,000 h^{-1}	Březina et al. (2020)
MnO(3 × 3)	100% (350°C)	80% (350°C)	200 ppm CO, 200 ppm C_3H_6, 10% O_2, WHSV = 60,000 ml g^{-1}·h^{-1}	In this work

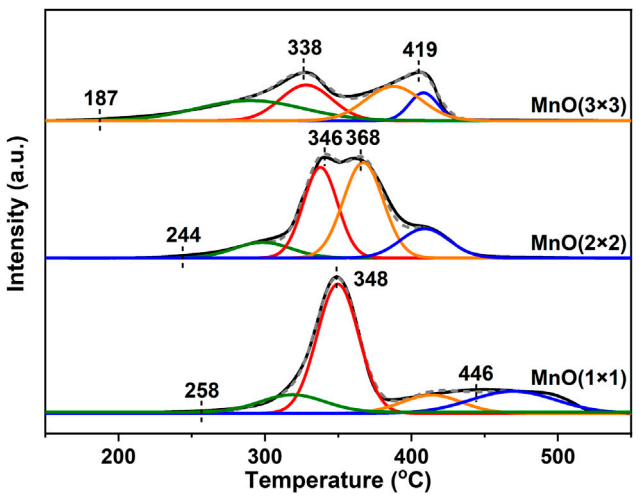

FIGURE 6 | H_2-TPR profiles of MnO(1 × 1), MnO(2 × 2), and MnO(3 × 3).

curves. According to the previous reports, the H_2-consumption peak at relatively lower temperature possibly represented the reduction of MnO_2 or Mn_2O_3 to Mn_3O_4, and the high temperature one be assigned to the further reduction of Mn_3O_4 to MnO (Gao et al., 2016). Moreover, it could be found that the initial reduction temperature of the low-temperature H_2-consumption peak of MnO(3 × 3) began at 187°C and centered at 338°C, which were about 70°C lower than those of MnO(1 × 1) and MnO (2 × 2), indicating that the redox recycling of Mn^{4+}/Mn^{3+} was more easily to occur on MnO(3 × 3) catalyst. As shown in **Table 3**, the amount of H_2 consumptions decreased from 11.03 to 7.42 mmol g^{-1} in the order of MnO(1 × 1) > MnO(2 × 2) > MnO(3 × 3). However, when the H_2 consumptions were normalized by the corresponding contents of manganese, the relative ratios were about 0.15 for all three catalysts, indicating the similar reduction amount of all MnO_x catalysts. As reported previously, the catalytic oxidation of C_xH_y on manganese oxides was mainly proceeded by the Mars-van Krevelen mechanism (Shen et al., 1993; Fleischer and Richmond, 1943), in which the lattice oxygen species reacted with C_xH_y, and the reduced manganese oxides were re-oxidized by gaseous oxygen. As a result, the C_xH_y oxidation activity of manganese oxides was mainly determined by its redox performance. Summarzing the above results, it seemed reasonably to suggest that the excellent reducibility of MnO(3 × 3) at low temperatures played the dominated factor for its best C_3H_6 oxidation activity. More importantly, it was not difficult to see that MnO(3 × 3), which had the best propylene oxidation activity, had a lower initial reduction temperature than MnO(1 × 1) and MnO(2 × 2). Accordingly, it could be concluded that the redox properties at low temperatures were more important for improving catalytic oxidation performance.

As reported by Ma et al. (Ma et al., 2018), the CO oxidation performance is extremely related to the interaction between the CO molecules and the active lattice oxygen of the catalysts. Therefore, the CO-TPR experiment was conducted on MnO(1 × 1), MnO(2 × 2), and MnO(3 × 3) to further determine the reactivity of lattice oxygen species. As shown in **Figure 7**, two CO-consumption peaks were observed on these three samples, suggesting two types of lattice oxygen with different reactivity (Shen et al., 1993). The peak at lower temperature range was ascribed to the reduction of MnO_2 to Mn_3O_4 (Shen et al., 1993; Fleischer and Richmond, 1943), while the peak at higher

TABLE 3 | The redox properties of various catalysts.

Sample	Mn contents (wt%)[a]	Mn^{3+}/Mn^{4+}[b]	$O_{ads}/(O_{ads} + O_{latt})$[c]	H_2 consumptions (mmol g^{-1})	H_2 consumptions/Mn contents
MnO(1 × 1)	64.2	0.71	0.21	11.03	0.17
MnO(2 × 2)	63.8	1.31	0.24	9.55	0.15
MnO(3 × 3)	56.9	1.54	0.29	7.42	0.13

[a]*The Mn contents of as-preapred sampls were determined by ICP.*
[b]*Calculated by the fitting results of Mn 2p XPS.*
[c]*Calculated by the fitting results of O 1s XPS.*

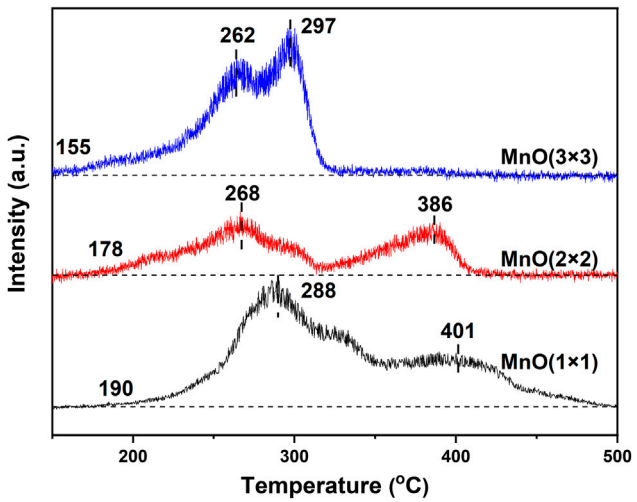

FIGURE 7 | CO-TPR profiles of MnO(1 × 1), MnO(2 × 2), and MnO(3 × 3).

temperature range was attributed to the reduction of Mn_3O_4 to MnO. Similar to the results of H_2-TPR, it can be seen clearly that the initial reduction temperatures of the low-temperature reduction peak, as well as the peak center on MnO(3 × 3) was still slightly lower than those on MnO(1 × 1) and MnO(2 × 2). The excellent low-temperature redox property of MnO(3 × 3) should be one of the main reasons for the best catalytic oxidation activity.

The Chemical States of Surface Species (XPS)

XPS was performed to identify the chemical state of surface elements. The Mn 2p spectra are shown in **Figure 8A**. Mn $2p_{3/2}$ and Mn $2p_{1/2}$ XPS peaks were centered at 642.3 and 654.1 eV, respectively, with the separation energy of 11.8 eV, close to that of Mn 2p XPS with an octahedral coordination in MnO_2 (Liu P. et al., 2018). The peaks at 654.7 and 643.5 eV were attributed to Mn^{4+}, and the peaks at 653.5 and 642.1 eV were attributed to Mn^{3+}. The mixed valence in catalysts was important for electron transport because the efficiencies of catalysts were usually governed by their ability and tendency to cycle between different valence states of the relevant cationic ions (Sun et al., 2011; Fang et al., 2017). Thus, the ratio of Mn^{3+}/Mn^{4+}

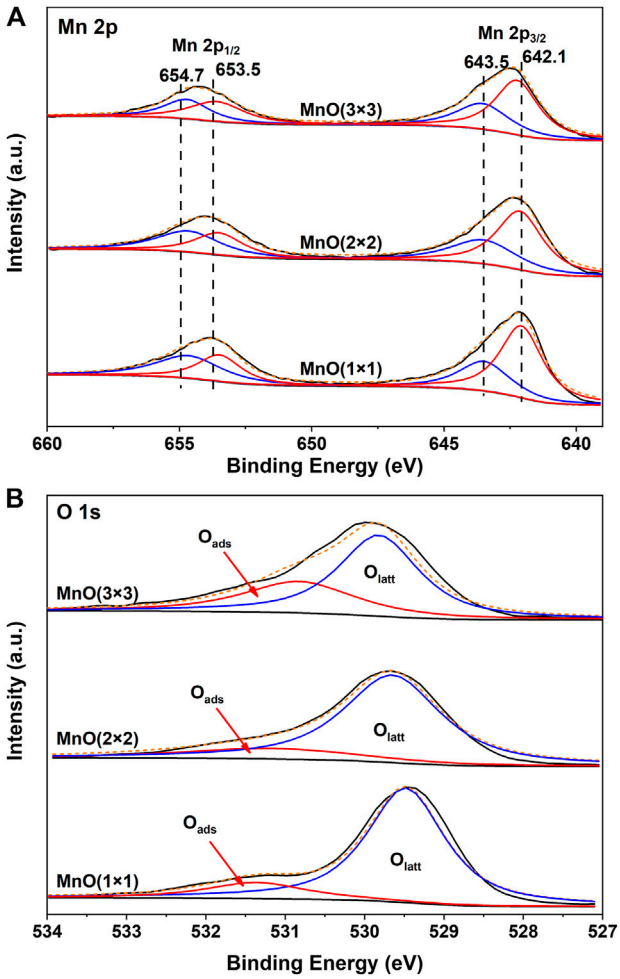

FIGURE 8 | XPS spectra of Mn 2p **(A)** and O 1s **(B)** for MnO(1 × 1), MnO(2 × 2), and MnO(3 × 3).

was calculated as a parameter to compare the catalytic activity of MnO_x samples. As calculated from **Figure 8A**, MnO(1 × 1) possessed the lowest Mn^{3+}/Mn^{4+} ratio of 0.73 (**Table 3**). When tunnel size increased from 0.23 to 0.69 nm, the ratio of Mn^{3+}/Mn^{4+} increased from 0.71 to 1.54, which indicated that more Mn^{3+} formed on MnO(3 × 3). More surface Mn^{3+} ions were always related to the formation of more surface oxygen vacancies on MnO_2, which was beneficial to the adsorption,

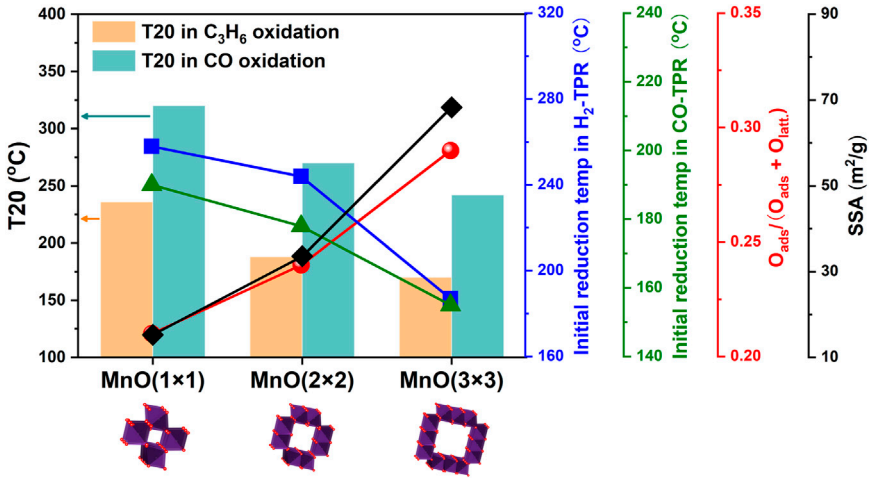

FIGURE 9 | The relationship between the catalytic oxidation activity and the results of H_2-TPR, CO-TPR, XPS, as well as the structural/textural properties.

activation and migration of oxygen species. Such a conclusion was further proven by the XPS results of O 1s. As shown in **Figure 8B**, two peaks centered at 529.5 and 531.4 eV were observed. The peak at *ca.* 529.5 eV was corresponded to surface lattice oxygen (O_{latt}), while the latter peak at *ca.* 531.4 eV was attributed to surface adsorbed oxygen (O_{ads}) (Galakhov et al., 2002; Wang W. et al., 2012). As shown in **Table 3**, the ratio of surface adsorbed oxygen species ($O_{ads}/(O_{latt} + O_{ads})$) on MnO(1 × 1), MnO(2 × 2), and MnO(3 × 3) were 0.27, 0.31 and 0.41, respectively. MnO(3 × 3) possessed the most abundant surface adsorbed oxygen species. The formation of adsorbed oxygen species are most likely resulted from the presence of surface oxygen vacancies on the different tunnel size MnO_2 catalysts. Surface active oxygen species played an important role in oxidation reactions (Tang et al., 2008; Widmann and Behm, 2011). Abundant surface adsorbed oxygen species were easily stripped at low temperatures and were favorable for stronger reducibility to enhance the oxidation performance, well consistent with the results of H_2-TPR. In other words, the abundant surface oxygen vacancies and surface adsorbed oxygen species dramatically facilitated the redox properties at low temperature, and then promoted its catalytic oxidation activity.

Relationship Between Catalytic Performance and Catalysts Properties

To further reveal the reasons for the most superior catalytic oxidation activity on MnO(3 × 3), the results of catalytic performance test, H_2-TPR, CO-TPR, XPS, as well as the structural/textural properties were re-organized in **Figure 9**. Here, T20, the temperature at which C_3H_6/CO conversion were 20%, was selected to represent the catalytic oxidation activity of MnO(1 × 1), MnO(2 × 2) and MnO(3 × 3), and lower T20 meant higher catalytic oxidation activity. As far as we know, for some important catalytic reactions, the increase of the specific surface area of support was beneficial to provide more active sites, which could lead the activity to increase. Taking into account the previous research about the tunnel sizes of these three MnO catalysts, N_2 can be adsorbed throughout the tunnel of MnO(3 × 3), partially adsorbed in the tunnel of MnO(2 × 2), and excluded from the tunnel of MnO(1 × 1). This indicated that the SSA results from the N_2 adsorption-desorption isotherms in our study reflected the effective adsorption sites of the MnO catalysts, *i.e.*, the effective catalytic oxidation sites. It could be considered that MnO(3 × 3) with the largest tunnel size and the biggest SSA was in favor of the catalytic oxidation performance (Waterhouse et al., 2003). Other than the optimal tunnel structures and higher SSA of MnO(3 × 3), it was found that the enhanced catalytic oxidation activity of MnO(3 × 3) was more related to its excellent redox property. Lower initial reduction temperatures in H_2/CO-TPR were always related to better redox properties. In this work, lower initial reduction temperatures in H_2/CO-TPR were achieved on MnO(3 × 3), meaning that the oxygen species on MnO(3 × 3) were more reactive. The higher concentration of surface adsorbed oxygen species on MnO(3 × 3) suggested the formation of more oxygen vacancies, which could significantly facilitate the adsorption and activation of oxygen during the reaction. In short, the optimal tunnel structure, highest SSA, and most superior redox properties accounted for the best catalytic oxidation activity of MnO(3 × 3). Through the above-mentioned comparative studies, a structure-activity relationship was well established.

CONCLUSION

In this work, three kinds of manganese oxides: MnO(1 × 1), MnO(2 × 2), and MnO(3 × 3) with different tunnel structures were prepared by a hydrothermal method. MnO(3 × 3) showed

much superior catalytic oxidation activity than MnO(1 × 1) and MnO(2 × 2). Through a series of characterizations, a structure-activity relationship was established that the unique tunnel structure, higher specific surface area, and better redox properties on MnO(3 × 3) accounted for its best catalytic oxidation activity. This work provides a new strategy for designing highly efficient catalytic oxidation catalysts through tuning the tunnel structures of metal oxide catalysts.

DATA AVAILABILITY STATEMENT

The original contributions presented in the study are included in the article/Supplementary Material, further inquiries can be directed to the corresponding authors.

AUTHOR CONTRIBUTIONS

XW: Methodology, Validation, Investigation, Writing—original draft. WT: Writing—review and editing. KG: Methodology. JJ: Methodology. FG: Conceptualization, Validation, Writing—review and editing, Supervision, Funding acquisition. QT: Conceptualization, Validation, Writing—review and editing. LD: Resources, Supervision, Project administration.

FUNDING

The finial support from the National Natural Science Foundation of China (No. 21972063) and Natural Science Foundation of Jiangsu Province (BK20200012).

REFERENCES

Breck, D. (1974). *Zeolite Molecular Sieves – Structure, Chemistry, and Use*. New York: Wiley-Interscience.

Brock, S. L., Duan, N. G., Tian, Z. R., Giraldo, O., Zhou, H., and SuibA, S. L. (1998). Review of Porous Manganese Oxide Materials. *Chem. Mater.* 10, 2619–2628. doi:10.1021/cm980227h

Březina, J., Pečinka, R., Boutikos, P., and Kočí, P. (2020). Comparison of Dual CO Light-Off Effect on Pt/CeO_2/γ-Al_2O_3, Pd/CeO_2/γ-Al_2O_3, Pt/γ-Al_2O_3 and Pd/γ-Al_2O_3 in the Presence of C_3H_6. *Chem. Eng. Sci.* 218, 115542–115550. doi:10.1016/j.ces.2020.115542

Carrillo, C., DeLaRiva, A., Xiong, H., Peterson, E. J., Spilde, M. N., Kunwar, D., et al. (2017). Regenerative Trapping: How Pd Improves the Durability of Pt Diesel Oxidation Catalysts. *Appl. Catal. B: Environ.* 218, 581–590. doi:10.1016/j.apcatb.2017.06.085

Chen, T., Dou, H. Y., Li, X. L., Tang, X. F., Li, J. H., and Hao, J. M. (2009). Tunnel Structure Effect of Manganese Oxides in Complete Oxidation of Formaldehyde. *Microporous Mesoporous Mater.* 122, 270–274. doi:10.1016/j.micromeso.2009.03.010

Ching, S., and Roark, J. L. (1997). Sol-Gel Route to the Tunneled Manganese Oxide Cryptomelane. *Chem. Mater.* 9, 750–754. doi:10.1021/cm960460k

Fang, J., Li, J., Gao, L., Jiang, X., Zhang, J., Xu, A., et al. (2017). Synthesis of OMS-2/graphite Nanocomposites with Enhanced Activity for Pollutants Degradation in the Presence of Peroxymonosulfate. *J. Colloid Interf. Sci.* 494, 185–193. doi:10.1016/j.jcis.2017.01.049

Fleischer, M., and Richmond, W. E. (1943). The Manganese Oxide Minerals: A Preliminary Report. *Econ. Geol.* 38, 269–286. doi:10.2113/gsecongeo.38.4.269

Galakhov, V., Demeter, M., Bartkowski, S., Neumann, M., Ovechkina, N., Kurmaev, E., et al. (2002). Mn 3s Exchange Splitting in Mixed-Valence Manganites. *Phys. Rev. B* 65, 113102. doi:10.1103/PhysRevB.65.113102

Gao, J. J., Jia, C. M., Zhang, L. P., Wang, H. M., Yang, Y. H., Hung, S. F., et al. (2016). Tuning Chemical Bonding of MnO_2 through Transition-Metal Doping for Enhanced CO Oxidation. *J. Catal.* 341, 82–90. doi:10.1016/j.jcat.2016.06.009

Golden, D. C., Chen, C. C., and Dixon, J. B. (1985). Synthesis of Todorokite. *Science* 231, 717–719. doi:10.1126/science.231.4739.717

Hazlett, M. J., Moses-Debusk, M., Parks, J. E., II, Allard, L. F., and Epling, W. S. (2017). Kinetic and Mechanistic Study of Bimetallic Pt-Pd/Al_2O_3 Catalysts for CO and C_3H_6 Oxidation. *Appl. Catal. B: Environ.* 202, 404–417. doi:10.1016/j.apcatb.2016.09.034

Heo, I., Schmieg, S. J., Oh, S. H., Li, W., Peden, C. H. F., Szanyi, J., et al. (2018). Improved Thermal Stability of a Copper-Containing Ceria-Based Catalyst for Low Temperature CO Oxidation under Simulated Diesel Exhaust Conditions. *Catal. Sci. Technol.* 8, 1383–1394. doi:10.1039/c7cy02288c

Huang, L., Hu, X. N., Yuan, S., Li, H. R., Yan, T. T., Shi, L. Y., et al. (2017). Photocatalytic Preparation of Nanostructured MnO_2-(Co_3O_4)/TiO_2 Hybrids: The Formation Mechanism and Catalytic Application in SCR deNO(x) Reaction. *Appl. Catal. B: Environ.* 203, 778–788. doi:10.1016/j.apcatb.2016.10.071

Huang, Z., Gu, X., Cao, Q., Hu, P., Hao, J., Li, J., et al. (2012). Catalytically Active Single-Atom Sites Fabricated from Silver Particles. *Angew. Chem. Int. Ed.* 124, 4274–4279. doi:10.1002/ange.201109065

Jarrige, J., and Vervisch, P. (2009). Plasma-enhanced Catalysis of Propane and Isopropyl Alcohol at Ambient Temperature on a MnO_2-Based Catalyst. *Appl. Catal. B: Environ.* 90, 74–82. doi:10.1016/j.apcatb.2009.02.015

Khosravi, M., Sola, C., Abedi, A., Hayes, R. E., Epling, W. S., and Votsmeier, M. (2014). Oxidation and Selective Catalytic Reduction of NO by Propene over Pt and Pt:Pd Diesel Oxidation Catalysts. *Appl. Catal. B: Environ.* 147, 264–274. doi:10.1016/j.apcatb.2013.08.034

Kijima, N., Ikeda, T., Oikawa, K., Izumi, F., and Yoshimura, Y. (2004). Crystal Structure of an Open-Tunnel Oxide α-MnO_2 Analyzed by Rietveld Refinements and MEM-Based Pattern Fitting. *J. Solid State. Chem.* 177, 1258. doi:10.1016/j.jssc.2003.10.038

Kim, C. H., Qi, G., Dahlberg, K., and Li, W. (2010). Strontium-doped Perovskites Rival Platinum Catalysts for Treating NOx in Simulated Diesel Exhaust. *Science* 327, 1624–1627. doi:10.1126/science.1184087

Leistner, K., Braga, C. G., Kumar, A., Kamasamudram, K., and Olsson, L. (2019). Volatilisation and Subsequent Deposition of Platinum Oxides from Diesel Oxidation Catalysts. *Appl. Catal. B: Environ.* 241, 338–350. doi:10.1016/j.apcatb.2018.09.022

Li, P., Chen, X., Li, Y., and Schwank, J. W. (2021). Effect of Preparation Methods on the Catalytic Activity of $La_{0.9}Sr_{0.1}CoO_3$ Perovskite for CO and C_3H_6 Oxidation. *Catal. Today* 364, 7–15. doi:10.1016/j.cattod.2020.03.012

Li, P., Chen, X., Ma, L., Bhat, A., Li, Y., and Schwank, J. W. (2019). Effect of Ce and La Dopants in Co_3O_4 Nanorods on the Catalytic Activity of CO and C_3H_6 Oxidation. *Catal. Sci. Technol.* 9, 1165–1177. doi:10.1039/c8cy02460j

Liu, F., Rong, S. P., Zhang, P. Y., and Gao, L. L. (2018). One-step Synthesis of Nanocarbon-Decorated MnO_2 with Superior Activity for Indoor Formaldehyde Removal at Room Temperature. *Appl. Catal. B: Environ.* 235, 158–167. doi:10.1016/j.apcatb.2018.04.078

Liu, P., Duan, J. H., Ye, Q., Mei, F. M., Shu, Z. H., and Chen, H. P. (2018). Promoting Effect of Unreducible Metal Doping on OMS-2 Catalysts for Gas-phase Selective Oxidation of Ethanol. *J. Catal.* 367, 115–125. doi:10.1016/j.jcat.2018.09.007

Liu, S., Wu, X. D., Weng, D., Li, M., and Fan, J. (2013). Sulfation of Pt/Al_2O_3 Catalyst for Soot Oxidation: High Utilization of NO_2 and Oxidation of Surface Oxygenated Complexes. *Appl. Catal. B: Environ.* 138, 199–211. doi:10.1016/j.apcatb.2013.02.053

Liu, S., Wu, X. D., Weng, D., Li, M., and Ran, R. (2015). Roles of Acid Sites on Pt/H-ZSM5 Catalyst in Catalytic Oxidation of Diesel Soot. *ACS Catal.* 5, 909–919. doi:10.1021/cs5018369

Liu, Y., Zong, W. J., Zhou, H., Wang, D. S., Cao, R. R., Zhan, J. J., et al. (2018). Tuning the Interlayer Cations of Birnessite-type MnO_2 to Enhance its Oxidation Ability for Gaseous Benzene with Water Resistance. *Catal. Sci. Technol.* 8, 5344–5358. doi:10.1039/c8cy01147h

Liu, Z., Li, Z., Chu, X., Shao, Y., Li, K., Chen, X., et al. (2020). B-Site Modification of $LaMn_{0.9}Co_{0.1}O_3$ Perovskite Using a Selective Dissolution Method in C_3H_6 Oxidation. *Catal. Sci. Technol.* 10, 6464–6467. doi:10.1039/d0cy01381a

Ma, L., Seo, C. Y., Chen, X., Sun, K., and Schwank, J. W. (2018). Indium-doped Co_3O_4 Nanorods for Catalytic Oxidation of CO and C_3H_6 towards Diesel Exhaust. *Appl. Catal. B: Environ.* 222, 44–58. doi:10.1016/j.apcatb.2017.10.001

Makwana, V. D., Son, Y. C., Howell, A. R., and Suib, S. L. (2002). The Role of Lattice Oxygen in Selective Benzyl Alcohol Oxidation Using OMS-2 Catalyst: A Kinetic and Isotope-Labeling Study. *J. Catal.* 210, 46–52. doi:10.1006/jcat.2002.3680

Miao, L., Nie, Q., Wang, J. L., Zhang, G. K., and Zhang, P. Y. (2019). Ultrathin MnO_2 Nanosheets for Optimized Hydrogen Evolution via Formaldehyde Reforming in Water at Room Temperature. *Appl. Catal. B: Environ.* 248, 466–476. doi:10.1016/j.apcatb.2019.02.047

Ooi, K., Miyai, Y., and Katoh, S. (1987). Ion-Exchange Properties of Lon-Sieve-type Manganese Oxides Prepared by Using Different Kinds of Introducing Ions. *Sep. Sci. Technol.* 22, 1779–1789. doi:10.1080/01496398708058434

Qi, F., Hirofumi, K., and Kenta, O. (1999). Manganese Oxide Porous Crystals. *J. Mater. Chem.* 9, 319–333. doi:10.1039/a805369c

Qi, F., Kanoh, H., Yoshitaka, M., and Kenta, O. (1995). Metal Ion Extraction Insertion Reactions with Todorokite Type Manganese Oxide in the Aqueous Phase. *Chem. Mater.* 7, 1722–1727. doi:10.1021/cm00057a023

Raj, R., Harold, M. P., and Balakotaiah, V. (2015). Steady-state and Dynamic Hysteresis Effects during Lean Co-oxidation of CO and C_3H_6 over Pt/Al_2O_3 Monolithic Catalyst. *Chem. Eng. J.* 281, 322–333. doi:10.1016/j.cej.2015.06.057

Ren, G. Q., Tang, Y., Liu, K. P., Su, Y., Miao, S., Liu, W., et al. (2018). Exceptional Antisintering Gold Nanocatalyst for Diesel Exhaust Oxidation. *Nano. Lett.* 18, 6489–6493. doi:10.1021/acs.nanolett.8b03003

Rida, K., Benabbas, A., Bouremmad, F., Pena, M. A., and Martı´nez-Arias, A. (2006). Surface Properties and Catalytic Performance of $La_{1-x}Sr_xCrO_3$ Perovskite-type Oxides for CO and C_3H_6 Combustion. *Catal. Commun.* 7, 963–968. doi:10.1016/j.catcom.2006.04.011

Seo, Y., Lee, M. W., Kim, H. J., Choung, J. W., Jung, C. H., Kim, C. H., et al. (2021). Effect of Ag Doping on Pd/Ag-CeO_2 Catalysts for CO and C_3H_6 Oxidation. *J. Hazard. Mater.* 415, 125373. . In Press. doi:10.1016/j.jhazmat.2021.125373

Shen, X. F., Ding, Y. S., Liu, J., Cai, J., Laubernds, K., Zerger, R. P., et al. (2005). Control of Nanometer-Scale Tunnel Sizes of Porous Manganese Oxide Octahedral Molecular Sieve Nanomaterials. *Adv. Mater.* 17, 805–809. doi:10.1002/adma.200401225

Shen, Y. F., Zerger, R. P., DeGuzman, R. N., Suib, S. L., McCurdy, L., Potter, D. 1., et al. (1993). Manganese Oxide Octahedral Molecular Sieves Preparation, Characterization, and Applications. *Science* 260, 511–515. doi:10.1126/science.260.5107.511

Shi, Q. L., Liu, T. Z., Li, Q., Xin, Y., Lu, X. X., Tang, W. X., et al. (2019). Multiple Strategies to Decrease Ignition Temperature for Soot Combustion on Ultrathin MnO_2-X Nanosheet Array. *Appl. Catal. B: Environ.* 246, 312–321. doi:10.1016/j.apcatb.2018.12.078

Shiley, T., and Buseck, P. R. (1981). Todorokites A New Family of Naturally Occurring Manganese Oxides. *Science* 212, 1024–1026. doi:10.1126/science.212.4498.1024

Sun, H., Chen, S., Wang, P., and Quan, X. (2011). Catalytic Oxidation of Toluene over Manganese Oxide Octahedral Molecular Sieves (OMS-2) Synthesized by Different Methods. *Chem. Eng. J.* 178, 191–196. doi:10.1016/j.cej.2011.10.047

Tan, W., Alsenani, H., Xie, S., Cai, Y., Xu, P., Liu, A., et al. (2020). Tuning Single-atom Pt_1-CeO_2 Catalyst for Efficient CO and C_3H_6 Oxidation: Size Effect of Ceria on Pt Structural Evolution. *ChemNanoMat* 6, 1797–1805. doi:10.1002/cnma.202000431

Tan, W., Liu, A., Xie, S., Yan, Y., Shaw, T. E., Pu, Y., et al. (2021). Ce-Si Mixed Oxide: A High Sulfur Resistant Catalyst in the NH_3-SCR Reaction through the Mechanism-Enhanced Process. *Environ. Sci. Technol.* 55 (6), 4017–4026. doi:10.1021/acs.est.0c08410

Tang, X., Chen, J., Huang, X., Xu, Y., and Shen, W. (2008). Pt/MnO_x-CeO_2 Catalysts for the Complete Oxidation of Formaldehyde at Ambient Temperature. *Appl. Catal. B: Environ.* 81, 115–121. doi:10.1016/j.apcatb.2007.12.007

Tang, X. F., Li, J. H., Sun, L. A., and Hao, J. M. (2010). Origination of N_2O from NO Reduction by NH_3 over Beta-MnO_2 and Alpha-Mn_2O_3. *Appl. Catal. B: Environ.* 99, 156–162. doi:10.1016/j.apcatb.2010.06.012

Tang, X. F., Li, Y. G., Huang, X. M., Xu, Y. D., Zhu, H. Q., Wang, J. G., et al. (2006). MnO_x-CeO_2 Mixed Oxide Catalysts for Complete Oxidation of Formaldehyde: Effect of Preparation Method and Calcination Temperature. *Appl. Catal. B: Environ.* 62, 265–273. doi:10.1016/j.apcatb.2005.08.004

Uematsu, T., Miyamoto, Y., Ogasawara, Y., Suzuki, K., Yamaguchi, K., and Mizuno, N. (2016). Molybdenum-doped α-MnO_2 as an Efficient Reusable Heterogeneous Catalyst for Aerobic Sulfide Oxygenation. *Catal. Sci. Technol.* 6, 222–233. doi:10.1039/c5cy01552a

Wang, F., Dai, H., Deng, J., Bai, G., Ji, K., and Liu, Y. (2012). Design and Synthesis of Porous Non-noble Metal Oxides for Catalytic Removal of VOCs. *Environ. Sci. Technol.* 46, 4034–4041. doi:10.1007/s11426-015-5469-8

Wang, H., Dong, J., Allard, L. F., Lee, S., Oh, S., Wang, J., et al. (2019). Single-site Pt/La-Al_2O_3 Stabilized by Barium as an Active and Stable Catalyst in Purifying CO and C_3H_6 Emissions. *Appl. Catal. B: Environ.* 244, 327–339. doi:10.1016/j.apcatb.2018.11.034

Wang, J. L., Li, J. E., Jiang, C. J., Zhou, P., Zhang, P. Y., and Yu, J. G. (2017). The Effect of Manganese Vacancy in Birnessite-type MnO_2 on Room-Temperature Oxidation of Formaldehyde in Air. *Appl. Catal. B: Environ.* 204, 147–155. doi:10.1016/j.apcatb.2016.11.036

Wang, W., McCool, G., Kapur, N., Yuan, G., Shan, B., Nguyen, M., et al. (2012). Mixed-phase Oxide Catalyst Based on Mn-Mullite (Sm, Gd) Mn_2O_5 for NO Oxidation in Diesel Exhaust. *Science* 337, 832–835. doi:10.1126/science.1225091

Wang, X., and Li, Y. D. (2002). Selected-control Hydrothermal Synthesis of Alpha- and Beta-MnO_2 Single Crystal Nanowires. *J. Am. Chem. Soc.* 124, 2880–2881. doi:10.1021/ja0177105

Waterhouse, G. I. N., Bowmaker, G. A., and Metson, J. B. (2003). Microfaceting and Thermodynamic Stability of the Surface under Chemisorption Conditions. *Appl. Surf. Sci.* 214, 36–51. doi:10.1007/s10975-005-0075-y

Widmann, D., and Behm, R. J. (2011). Active Oxygen on a Au/TiO_2 Catalyst: Formation, Stability, and CO Oxidation Activity. *Angew. Chem. Int. Ed.* 50, 10241–10245. doi:10.1002/anie.201102062

Xu, R., Wang, X., Wang, D. S., Zhou, K. B., and Li, Y. D. (2006). Surface Structure Effects in Nanocrystal MnO_2 and Ag/MnO_2 Catalytic Oxidation of CO. *J. Catal.* 237, 426–430. doi:10.1016/j.jcat.2005.10.026

Zhou, J., Qin, L. F., Xiao, W., Zeng, C., Li, N., Lv, T., et al. (2017). Oriented Growth of Layered-MnO_2 Nanosheets over Alpha-MnO_2 Nanotubes for Enhanced Room-Temperature HCHO Oxidation. *Appl. Catal. B: Environ.* 207, 233–243. doi:10.1016/j.apcatb.2017.01.083

Conflict of Interest: The authors declare that the research was conducted in the absence of any commercial or financial relationships that could be construed as a potential conflict of interest.